JGR Oceans

RESEARCH ARTICLE

10.1029/2024JC020949

# Contrasting Methane Seepage Dynamics in the Hola Trough Offshore Norway: Insights From Two Different Summers

**Bénédicte Ferré[1], Thibaut Barreyre[2,3], Stefan Bünz[1], Claudio Argentino[1], Jorge Corrales-Guerrero[4], Knut Ola Dølven[1], Marie Stetzler[1], Luca Fallati[5], Muhammed Fatih Sert[1], Giuliana Panieri[1], Samuel Rastrick[4], Tina Kutti[4], and Manuel Moser[1]**

[1]Department of Geosciences, UiT the Arctic University of Norway, Tromsø, Norway, [2]Department of Earth Science/K.G. Jebsen Centre for Deep Sea Research, University of Bergen, Bergen, Norway, [3]Geo-Ocean, CNRS, Univ Brest, Ifremer, UMR6538, Plouzane, France, [4]Institute of Marine Research, Bergen, Norway, [5]Department of Earth and Environmental Sciences (DISAT), University of Milano-Bicocca, Milano, Italy

**Key Points:**

- A combination of warmer bottom water and low tide increases methane seeps 3.5 times by altering sediment gas solubility and pore pressure
- Intermittent seeps and strong oceanic currents explain the limited microbial mats and the low methane concentration in the water column
- We found sub-seafloor pathways for gas migration in methane seep areas, influenced by topography

**Supporting Information:**

Supporting Information may be found in the online version of this article.

**Correspondence to:**

B. Ferré,
benedicte.ferre@uit.no

**Citation:**

Ferré, B., Barreyre, T., Bünz, S., Argentino, C., Corrales-Guerrero, J., Dølven, K. O., et al. (2024). Contrasting methane seepage dynamics in the Hola trough offshore Norway: Insights from two different summers. *Journal of Geophysical Research: Oceans*, *129*, e2024JC020949. https://doi.org/10.1029/2024JC020949

Received 19 JAN 2024
Accepted 30 MAY 2024

**Author Contributions:**

**Conceptualization:** Bénédicte Ferré, Thibaut Barreyre
**Data curation:** Bénédicte Ferré, Thibaut Barreyre
**Formal analysis:** Bénédicte Ferré, Stefan Bünz, Marie Stetzler, Manuel Moser
**Funding acquisition:** Bénédicte Ferré
**Investigation:** Bénédicte Ferré
**Methodology:** Bénédicte Ferré, Thibaut Barreyre, Knut Ola Dølven
**Project administration:** Bénédicte Ferré
**Resources:** Bénédicte Ferré
**Supervision:** Bénédicte Ferré, Knut Ola Dølven, Samuel Rastrick, Tina Kutti
**Visualization:** Bénédicte Ferré
**Writing – original draft:** Bénédicte Ferré



**Abstract** This study investigates the temporal variations in methane concentration and flare activity in the Hola trough (offshore Norway) during May 2018 and June 2022. Between these time periods, methane seep activity exhibits 3.5 times increase, as evidenced by hydroacoustic measurements. As the seep area in the Hola trough is constantly within the hydrate stability zone, the observed increase cannot be attributed to migration of its shallow boundary due to temperature increase. However, a combination of low tide conditions resulting in a lower sediment pore pressure and a bottom water temperature increase resulting in a lower methane solubility is likely to explain the increase in the number of seeps observed in June 2022. The hypothesis of tide influence is supported by data collected from a piezometer deployed and recovered during the cruise showing that the tidal effect was observed 3 m below the seafloor. Despite the numerous methane seeps detected, methane concentration and gas flow rates near the seafloor were low (<19 nM and <70 mL $min^{-1}$, respectively) compared to other areas with methane seep activity. This is likely due to strong currents rapidly dispersing methane in the water column. Sub-seafloor investigations identified pathways for gas migration in methane seep areas, influenced by topography. This study provides valuable insights into the temporal dynamics of methane concentrations, flare activity, and gas distribution in the Hola trough, contributing to our understanding of offshore methane dynamics in the region.

**Plain Language Summary** The Hola Trough, offshore Norway's Lofoten-Vesterålen (LoVe) area, has been of interest for many years due to its rich marine life and potential oil and gas resources. There, coral mounds thrive around methane seepage. The LoVe observatory network monitors this unique environment. Using this observatory platform, associated data set and research expeditions at sea, the project EMAN7 (Environmental impact of Methane seepage and sub-seabed characterization at LoVe-Node 7) aims to understand the environmental impact of methane seepage as well as its spatio-temporal variability. The comparison of methane seep activity during two summers with different environmental conditions revealed 3.5 times more seeps when a combination of warmer bottom water and low tide changes the sediment pore properties. A sensor recording subseafloor pore pressure and bottom temperature supports these findings. Sub-seafloor investigations identified routes for gas migration in methane seep areas, influenced by topography.

## 1. Introduction

Methane ($CH_4$) is the second most abundant greenhouse gas after carbon dioxide ($CO_2$), yet it is 85 times more potent than $CO_2$ over a 20-year period (Myhre et al., 2013). Methane therefore contributes directly to global warming, but also indirectly because $CH_4$ oxidation produces $CO_2$. The Paris Agreement, signed by 196 Parties in December 2015, aimed to limit global temperature rise to less than 2°C above pre-industrial levels, and more recently, the Global Methane Pledge was signed by 103 countries, including 15 major emitters to reduce $CH_4$ emissions by 30% before 2030, compared to 2020 levels. Anthropogenic $CH_4$ contribution to atmospheric level is far greater than natural contribution; however, it is critical to better understand this natural input in order to constrain models aiming at calculating the impact of various scenarios proposed to reduce global warming.

The ocean is a potential source of $CH_4$ to the atmosphere, partly owing to $CH_4$ leaking through the seabed (Saunois et al., 2020). Methane seepages are widespread in continental margins worldwide (Judd & Hovland, 2007), and are major transport vectors of carbon from the Earth's sub-surface to the overlying ocean (Archer

**Writing – review & editing:** Bénédicte Ferré, Thibaut Barreyre, Stefan Bünz, Claudio Argentino, Jorge Corrales-Guerrero, Knut Ola Dølven, Marie Stetzler, Luca Fallati, Muhammed Fatih Sert, Giuliana Panieri, Samuel Rastrick

et al., 2009; Boetius & Wenzhöfer, 2013). Temporal constraints to seabed $CH_4$ emissions and controlling factors remain poorly known, as well as their fate in a changing ocean (Bindoff et al., 2019). Nonetheless, as $CH_4$ traps solar heat more efficiently than $CO_2$, concerns exist if this $CH_4$ reaches the sea surface and the atmosphere. In response to climate-driven changes in the physical environment, $CH_4$ emissions from subsurface hydrocarbon reservoirs may occur due to reduced stability in gas hydrates and marine permafrost. The release of $CH_4$ is also modulated by environmental parameters such as tide (e.g., Römer et al., 2016; Sultan et al., 2020), temperature changes (Berndt et al., 2014; Ferré et al., 2012, 2020) and more sporadic events such as tectonic stress (Franek et al., 2017). Methane is emitted from the sediment to the water column as free (bubble) or dissolved gas. Once in the water column, it can be consumed by microbes (e.g., Damm et al., 2005), dispersed by ocean currents (Silyakova et al., 2020), and transferred to the atmosphere (Shakhova et al., 2010)—a process that can be modulated by water column stratification (Myhre et al., 2016). Bubble properties also play a role in the potential $CH_4$ transfer to the atmosphere, that is, larger bubbles and surfactant-covered bubbles have a greater potential for rising higher in the water column than smaller and cleaner bubbles (Leifer & Patro, 2002; McGinnis et al., 2006).

A leading question concerning $CH_4$ release in the ocean is whether it affects carbonate chemistry at a regional scale (Biastoch et al., 2011). This question is especially relevant in seep areas where $CH_4$ is released due to dissociating gas hydrates or permafrost, then oxidized to $CO_2$ by microbial mechanisms. These perturbations in carbonate chemistry may endanger marine organisms that build their shells and skeletons from calcium carbonate (Orr et al., 2005) such as cold-water corals (CWCs). Conversely, CWCs may benefit from additional nutrient output from microbial productivity surrounding seeps (Hovland et al., 1998; Jensen et al., 2012). Furthermore, it has been suggested that the formation of these habitats may be driven by both hydrodynamic processes and the presence of authigenic carbonate substrate, indicative of past microbial activity at seeps (Becker et al., 2009).

Here we focus on the Hola Trough offshore Norway's Lofoten-Vesterålen (LoVe) area, where CWCs thrive around $CH_4$ seepage. With its LoVe observatory network (see Text S1 in Supporting Information S1) that monitors this unique environment, this area is an ideal location to study the influence of $CH_4$ on CWCs. The main goal of the project EMAN7 (Environmental impact of Methane seepage and sub-seabed characterization at LoVe-Node 7) is to investigate the influence of oceanic conditions on $CH_4$ seepage patterns at the Hola trough, the fate of $CH_4$ within the water column, as well as its potential contribution to ocean acidification and associated impact on both CWC reefs and associated biological communities. In addition, we aim to quantify the release of carbon from the seabed and reconstruct trends in $CH_4$ emissions. In this present study, we evaluate influencing factors for spatio-temporal variability of $CH_4$ emissions in the area by comparing hydroacoustic and oceanographic data obtained during two research cruises (CAGE 18-2 from 20–27 May 2018 and CAGE 22-3 from 8–15 June 2022). We also present the main observation of the seafloor, sub-seafloor and the CWCs. The cruises were performed in the frame of the CAGE Center of Excellence (Center for Arctic Gas Hydrate, Environment and Climate). Further components of the project will be presented in subsequent publications.

## 2. Study Area

Lofoten-Vesterålen, located on the Norwegian continental shelf, has been of interest for many years from oceanographic, biological and economic standpoints. Warm Atlantic water is transported to the Arctic via the narrow shelf and trough (Loeng, 1991), which is characterized by high turbulence and vertical mixing (Buhl-Mortensen et al., 2012). The vast spawning areas and fish stocks also provide highly productive fishery in this region (e.g., Misund & Olsen, 2013).

The main study area is located in Hola, a ∼12 km wide trough between the banks of Vesterålsgrunnen and Eggagrunnen (Figure 1). The trough was formed by the action of ice and later partly covered by fine-grained glaciomarine sediments. The seafloor is therefore mainly covered with sand, but also with gravelly sand, sandy gravel and coarser sediment. Giant Barchan-type sandwaves up to 3 km long, 7 m high, and up to 300 m apart are formed by strong currents (Bøe et al., 2009).

Lofoten is known for its strong tidal currents resulting from the interaction of large tidal amplitudes with the complex bathymetry of the region (Børve et al., 2021). These tidal currents are of great significance for marine life, as they facilitate nutrient-rich environments that attract various species of fish and other marine organisms. Winds, large-scale ocean circulation and local topography also influence the overall water movement in the region. Water masses are dominated by the Norwegian Coastal Water (NCW) brought by the Norwegian Coastal Current (NCC) flowing along the coast from the southwest and the Norwegian Atlantic Water (NAW) transported

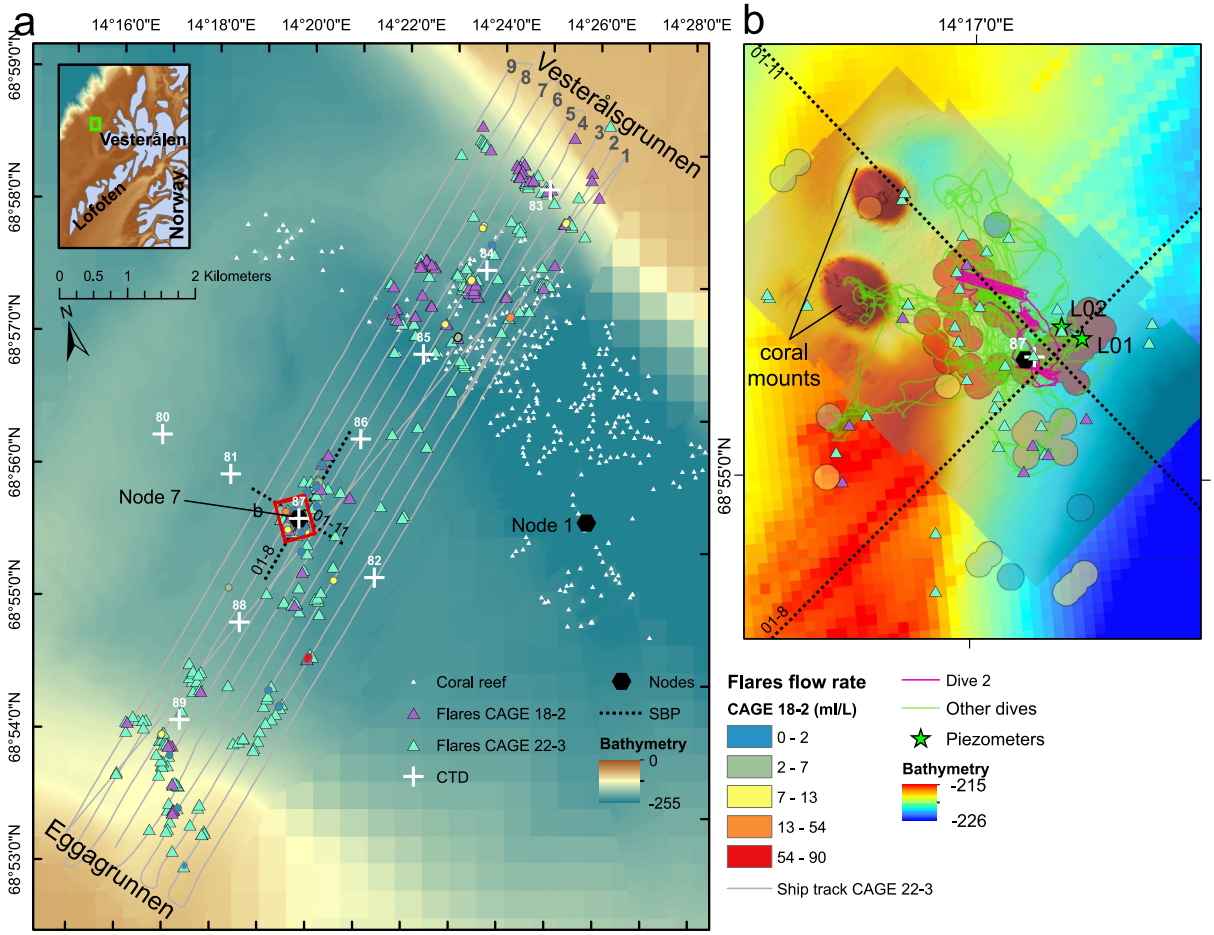


**Figure 1.** (a) Map of the area in the Hola trough, offshore Lofoten and Vesterålen islands (Norway, see green square in the inset map). The main map also shows the coral reef locations (white triangles), the sub-bottom profiles (SBP, black lines), the CTD casts (white crosses) and nodes 1 and 7 (large hexagons, node 7 being in the center of the figure). The flares detected from multibeam echosounder during CAGE 18-2 and CAGE 22-3 cruises are shown by purple and light blue triangles, respectively. The multibeam survey during both cruises is shown by the higher resolution of the bathymetry superimposed on the IBCAO bathymetry. The gray line shows the ship track during CAGE 22-3 that overlapped with CAGE 18-2, with each line number as mentioned in the text and in Figure 8. The colored dots and merged dots represent the flow rates from $CH_4$ seeps calculated using the method described in Veloso et al. (2015) during CAGE 18-2, using a new clustering method (Dølven, 2024, https://zenodo.org/records/11214460). (b) High-resolution microbathymetry obtained from the Remote Operated Vehicle (ROV), superimposed on the bathymetry obtained from the vessel. The two piezometers (L01 and L02) are represented by the green stars and the ROV tracks are represented by the green lines. We performed a photomosaic of the seafloor during dive two (pink line). SBP, CTD casts and flow rates from SBES during CAGE 18-2 are also indicated with the same color code as Figure 1a.

by the Norwegian Atlantic Current (NAC) which follows the continental slope. The NCW is colder (2–6°C) and fresher (average of 34.5 PSU) than NAW (traditionally defined with salinity greater than 35 PSU with temperatures of 6–9°C when it enters the Norwegian Sea, Blindheim, 1990). Both these currents are strong (>1 m $s^{-1}$, typically 0.2–0.4 m $s^{-1}$), and create a complex circulation pattern together with the strong local tides in the narrow trough (Bøe et al., 2009).

The $CH_4$ escaping the sediments at this site has a predominant thermogenic origin, as determined by isotopic and molecular composition of the gas (Sauer et al., 2015), and U/Th ages of $CH_4$-derived carbonate crusts indicated that this seepage system has been active for at least ~11 ky (Chand et al., 2008; Crémière et al., 2016). Bottom water $CH_4$ concentration has been estimated to be 42 nM (Sauer et al., 2015) in the near vicinity of the seeps, which is approximately 10 times higher than normal background concentrations and indicates that the anaerobic $CH_4$ oxidation (AOM) in the sediment provides a limited $CH_4$ filter.

Microbial mats and tubeworms are typical of Arctic seep environments (e.g., Argentino et al., 2022) and are found in this area in association with extensive pavements of $CH_4$-derived carbonates forming due to the high alkalinity

generated by AOM (Crémière et al., 2016; Sauer et al., 2017). These carbonate features offer a unique habitat for chemosynthetic ecosystems (Niemann et al., 2006) and they can be colonized by corals and sponges, bivalves and chemosynthesis-based communities (Sibuet & Roy, 2002). The Hola trough is indeed also known for a large amount of CWCs *Desmophyllum pertusum* (*Lophelia pertusa)* immediately east of the sandwaves (Bøe et al., 2009).

## 3. Material and Methods

We performed CTD (Conductivity, Temperature, Depth) casts and water sampling as well as hydroacoustic surveys during two research cruises in the Hola trough (Figure 1). The cruise CAGE 18-2 was conducted with the Research Vessel (R/V) *Helmer Hanssen* (*HH*) from 20–27 May 2018, and CAGE 22-3 with R/V *Kronprins Haakon* (*KPH*) from 8–15 June 2022. During CAGE 22-3, we also performed close-up work with the work-class Remote Operated Vehicle (ROV) Ægir6000 including video imaging and installation of two piezometers, as well as gas, sediment and coral sampling. We combine methodological approaches, data from R/Vs, as well as sub-surface data to provide an improved understanding of the temporal (seasonal and long-term) and spatial variability of $CH_4$ seeps and their environmental implications. The different equipment and settings used during both surveys are summarized in Table S1 in Supporting Information S1.

### 3.1. CTD and Water Column Sampling

On both R/Vs, an SBE 911plus CTD mounted on a rosette measures the vertical profiles of physical properties of seawater such as conductivity, temperature and pressure, from which we can derive salinity, density, depth and P-wave (sound) velocity. Additional sensors measure the turbidity, the fluorescence/chlorophyll, and the oxygen content. Twelve Niskin bottles of 5-L (*HH*) and 10-L (*KPH*) are attached to the rosette frame to collect water samples from chosen depths. We collected 187 water samples during CAGE 18-2 (15 casts, 9/12 levels) and 95 during CAGE 22-3 (12 casts, 7/8 levels) (Figure 1).

We applied the conventional headspace gas extraction technique to prepare water samples for measurements of $CH_4$ concentrations. Water samples were collected air-bubble-free into 120 mL crimp seal bottles once the CTD rosette was back on the ship and poisoned with 1 mL NaOH solution. Five ml of the sample were substituted with nitrogen gas, and the bottles were vigorously shaken to facilitate the equilibration of dissolved and headspace gas. The samples were kept in the refrigerator (5°C) until further analysis with the Gas Chromatographer—FID (ThermoScientific Trace 1,310). Dissolved methane concentrations in seawater samples (nmol $L^{-1}$ or nM) were calculated from the atmospheric equivalence of the headspace concentrations (ppm) using Henry's law and Bunsen solubility coefficients as a function of temperature and salinity which corresponds to the atmospheric equilibrium concentration of 3.2 nM at 34.8 psu and 6°C (Wiesenberg & Guinasso, 1979).

### 3.2. Hydroacoustic

Both R/Vs are equipped with Teledyne RD's "Ocean Surveyor" Acoustic Doppler Current Profilers (ADCP) that operate at narrowband and broadband frequencies, specifically at 150 and 38 kHz. The ADCP 150 kHz version is installed in a flush-mounted configuration. Data collection is facilitated through a deck unit that communicates with the device, and a standard computer located in the Instrument room. Only data from CAGE 22-3 are presented here.

R/V *HH* (used during CAGE 18-2) is equipped with a Kongsberg Simrad EK60 scientific singlebeam echosounder system (SBES). The high frequencies of SBES are sensitive to gas bubbles in the water column, and the rising bubbles appear as high amplitude anomalies (acoustic flares) in the water column. $CH_4$ flare flow rates were estimated from the SBES echograms at 38 kHz obtained during CAGE 18-2 using the mathematical relation between target strength (TS; a function of the acoustic backscatter intensity) and gas flow (Veloso et al., 2015, 2019), assuming spherical $CH_4$ bubbles. We used the software ESP3 (Ladroit et al., 2020) to process the echograms by selecting the TS of discernible acoustic flares (disregarding fish-like signals) within a 5–10 m layer above the seafloor to limit noise from seabed reverberation. We calculated the flow rates using the Virtual Bubble Analysis Lab (VBALab) pluggin, which follows the method of Veloso et al. (2015) implemented in ESP3. Because seeps can be insonified multiple times during hydroacoustic surveys, we clustered acoustic flares whose acoustic footprints overlap to avoid overestimating flow rates by double-counting flares. Flow rates of these clusters were calculated with gridded averaging (Dølven, 2024, https://zenodo.org/records/11214460). Briefly,

this method first calculates the flow per unit area for each clustered flare observation. In areas where flare observations overlap, the average flow per unit area of the overlapping observations is used. The total flow rate is then obtained by integrating over the total area. All flare observations within 1.9 times their average radius of two adjacent flares were clustered (Figure 1). A wrong setting on the singlebeam during CAGE 22-3 prevents us from comparing both data sets, and we could therefore only calculate the flow rates during CAGE 18-2.

Both vessels are equipped with Kongsberg EM-302 Multibeam echosounders (MBES) operating at a frequency of 30 kHz and providing high-resolution bathymetric data up to a water depth of 7,000 m. The system was used with a 60°/60° opening angle during CAGE 18-2 and 45°/45° during CAGE 22-3. The ping rate depends on the water depth and opening angle and switches frequently between 0.5 and 2 Hz. Throughout the surveys, the MBES consistently delivered uninterrupted bathymetric data, offering insights into the seafloor morphology in the research area. However, to prevent any disruptions with the acoustic instruments of the ROV, the MBES was not logging during ROV surveys. Another application of the MBES is to monitor the water column. The acquired data were analyzed using the QPS FMMidwater software. The analysis of water column data allows the detection of acoustic flares indicating gas seepage from the seafloor and the spatial distribution of detected flares on top of the bathymetry. To avoid counting flares multiple times, we removed flares within a radius of 10 m from each other (Figure 1). This buffer was chosen based on the flares observed in Fledermaus after selection in FMMidwater. The EM-302 also houses the Kongsberg SBP300-6 sub-bottom profiler (SBP) imaging the upper 10 s of meters of the sediment column. The SBP during CAGE 22-3 was set with a chirp pulse length of 50 ms and frequency bandwidth of 2.5–6.5 kHz (see Figure 1 for profile locations).

### 3.3. ROV Ægir6000

The ROV Ægir6000 is a work-class ROV 150 Hp equipped with samplers and sensors. It is deployed with a 750 m+ tether management system (TMS) and has seven cameras recording the environments from different angles. Positioning data for the ROV dives were obtained using the HIPAP 501 USBL (Ultra Short Base Line) high-precision underwater system. Using its manipulators, the Ægir6000 can retrieve specific samples from the seafloor and gather sediment samples with push and blade corers. It can also carry out various technical operations. Additionally, this ROV is equipped with coring tools, gas and water samplers, as well as oceanographic and geochemical sensors. During CAGE 22-3, the ROV was involved in several operations near node 7. Besides directly collecting samples from the seafloor, the ROV was used for high-resolution mapping of seafloor environments through MBES and photogrammetry. The ROV was equipped with the high-frequency EM 2040 (Simrad Kongsberg) MBES. MBES data were acquired along seven 250 m long transects flying 40 m above the seafloor, obtaining a microbathymetric image of an area of ~90,000 $m^2$ around node 7, including two coral mounds, with a 0.4 m/pixel resolution (Figure 1b). Data acquisition was planned and managed with EIVA NaviSuite® software, and raw MBES data were then processed and cleaned using EIVA NaviModel Producer®.

In addition, four specific areas were chosen for mapping using ROV photogrammetry with an ultra-high resolution. For this purpose, the ROV was fitted with a specialized photogrammetry tool containing an HD camera aimed directly downward at a 90° angle to the seafloor. Additionally, two extra strobes were installed to provide more than 2,500 W of illumination to the seafloor, ensuring uniform coverage. Finally, two deep-sea lasers were positioned 15 cm apart to complete the setup. The data were then imported and processed in Agisoft Metashape 1.8 Professional Edition® and processed following a well-established photogrammetric workflow (Fallati et al., 2020; Lim et al., 2020; Price et al., 2019) obtained Digital Elevation Models (DEMs) and orthomosaics, scaled and with a millimetric resolution (Fallati et al., 2023; Panieri et al., 2024).

### 3.4. Sub-Seafloor Pore Pressure

By definition, permeability sets the Darcy velocity of fluid flow subjected to a given pressure gradient. Permeability thus exerts a very strong modulation on the matter and heat fluxes associated with fluid circulation, as well as on venting velocity and temperature. The piezometers (i.e., pore pressure sensors) complement node 7 (Keller pressure sensor) to record sub-seafloor pore-water pressure and temperature within the sediment near the seeps over time. The objective is to investigate the pore-water pressure and thermal response to tidal loading and in combination with further poroelastic and thermal modeling to infer on the permeability structure and associated fluxes (Barreyre et al., 2018) of the sediment-hosted system at Hola. Ultimately, we aim at characterizing the distribution of outflow and quantifying the energy fluxes through the extrapolation of instrumental acquired time-

series data (e.g., velocity, temperature) combined with the surface area estimated from the photomosaic (e.g., Barreyre et al., 2012). This will provide us with two independent methods to estimate fluxes, one model-driven and another one data-driven. We have performed three piezometer deployments, one short-term (L01) in 2022 (during CAGE 22-3 cruise) and two long-term (L01 and L02) in 2022–2023. Piezometer L01 was deployed at 14° 17′09.6″E and 68°55′04.3″N, for both short-(about 3.5 days during CAGE 22-3, 2022) and long-term deployment (about 11 months, 2022–2023), and piezometer L02 at 14°17′07.8″E and 68°55′04.8′N, for long-term deployment (about 11 months, 2022–2023) (Figure 1b for location). The standpipes of the piezometer were installed via an installation rig of ∼6.3 m and 4 tons for guided penetration of OD 45 mm pipes using a 2.2 T deadweight. Once the rig was deployed on the seafloor, the deadweights were unlocked by the ROV, and re-locked after complete standpipe penetration. The rig was then lifted back to the vessel. The 3 m long piezometer standpipe consists in a filter tip (50 micron sintered), 45 mm OD steel pipe and hydraulic receptacle on top. During handling and installation, the hydraulic receptacle was protected by a dummy plug. The top part of the steel pipe was outfitted with anodes to minimize corrosion on vital parts. The loggerheads, which contain total pressure sensors, data logger and battery for standalone operation of the piezometer, were docked by the ROV to the hydraulic receptacle on the installed standpipe after recovery of the installation rig. Only the data from L01 will be presented here, and we compare them with data obtained from the Keller pressure sensor at node 7.

## 4. Results and Discussion

### 4.1. Observation From the ROV

The ROV performed a range of activities, such as mapping the area, collecting sediment and coral samples, and observing seeps. The seafloor predominantly consisted of bioclastic sediments, which originate from marine organisms like dead corals and shells. The grain size of surface sediment is heterogeneous, ranging from sands to boulders (Figure 2). Carbonate crusts form large pavements covered by a thin veneer of sediment, and are sporadically colonized by sponges, anemones and corals (Figure 2). White microbial mats are thinly distributed around the edges of carbonate crusts or in carbonate-free spots, indicating a limited sealing capacity of the carbonates which impedes the sulfide-rich fluids released by AOM to reach the seafloor and to sustain mat growth. The general lack of tubeworms in this seepage site is likely related to the coarse sediment composition, that is, the tubeworm species dominating the benthic community of nearby seeps from canyons on the lower continental slope off Lofoten–Vesterålen (Sen et al., 2019) require soft sediment settlement and continued growth. While cnidarians and sponges are common at node 7, no cnidarians and sponges were observed in the seeps studied by Sen et al. (2019), possibly due to the high sulphide concentration in bottom waters which makes the environment too toxic for non-endosymbiotic organisms. As expected, the most frequently observed coral species at node 7 was *Desmophyllum pertusum (Lophelia Pertusa)*, forming a coral patch of approximately $50 \times 30$ m$^2$ across, dominated by living coral polyps and an associated soft-coral community (Figure 2c). During a maintenance cruise that occurred in March 2023, a second coral patch ($10 \times 6$ m$^2$ across) was discovered in the northern corner of the node 7 study area. Further studies within this project will elucidate the plausible nutritional link between *D. pertusum* at the $CH_4$ seepage and the plausible impact of elevated $CO_2$ concentrations near the seepage areas on *D. pertusum* calcification rates.

One of the objectives of CAGE 22-3 was to measure the size and rising speed of bubbles using a system comprised of two perpendicular checkerboards that were intended to be placed in front of bubble streams. Despite extensive exploration over many hours, we only encountered small and sporadic bubbles that were challenging to detect from the ROV. Notably, bubble streams observed during our explorations would cease for a minimum of 30 min (the longest duration we waited for their return) and were of diminutive size. Bubble streams also seemed not to be constant, as the exact escape location could switch a few meters away after this time. This inconsistency of $CH_4$ source could explain the reduced microbial mats that lack time to fully develop before the release stops. To enhance the operation with the checkerboards, we disassembled the system and retained only one checkerboard, which we held steadily using the ROV's arm whenever we would see bubbles. Although this approach provides a preliminary assessment of bubble sizes, we estimated the bubbles to be smaller than a few mm in diameter (Figure 2d).

Gas composition and isotopic signatures were measured from gas collected using a bubble catcher held by the ROV. The $\delta^{13}C$ values of the different hydrocarbons provide insights into the source and processes involved in their formation. More negative $\delta^{13}C$ values typically suggest microbial sources, while less negative values can be

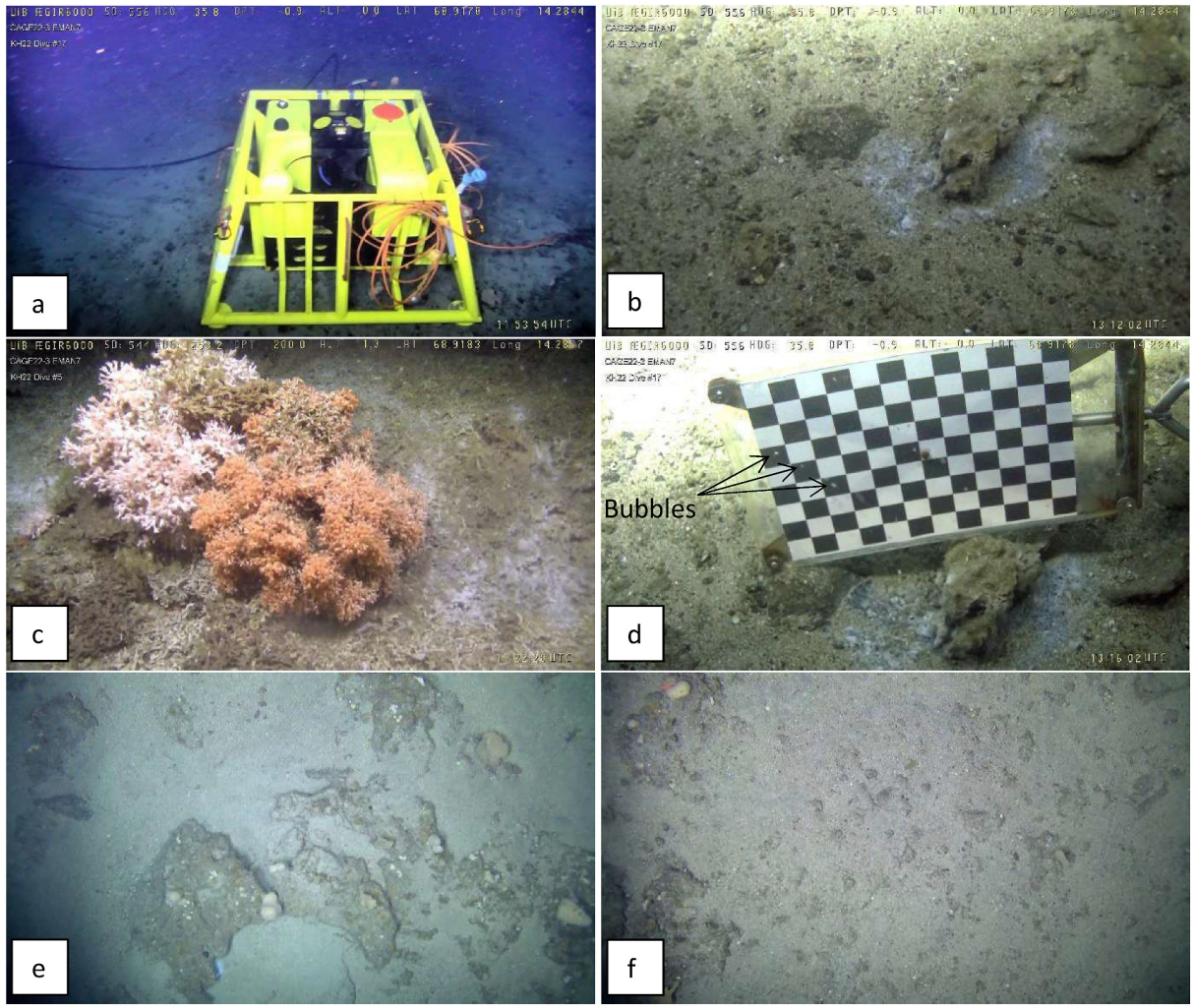


**Figure 2.** Snapshots of the seafloor taken by the ROV: (a) node 7 where the ADCP (center, three yellow beams) and the echosounder (red beam) are visible, (b) seafloor with carbonate crusts and microbial mats near node 7, (c) corals from the south coral mound, (d) checkerboard (grid 3 × 3 cm) showing the small bubbles rising, on top of a carbonate crust, (e) and (f) example of seafloor sediment.

associated with thermogenic sources (Whiticar, 1999). Here, bubbles were mostly composed of $CH_4$ (99.7%), ethane (0.15%) and propane (0.06%). Our $\delta^{13}C$ values for different hydrocarbons (c1 to c4) are between −46‰ for $CH_4$ and −23.5‰ for butane, which tends to thermogenic signature as previously found (Crémiere et al., 2016; Sauer et al., 2015) (Figure S1 in Supporting Information S1).

### 4.2. Comparison of Water Column Conditions and $CH_4$ Concentration

During both research cruises, we observed a relatively homogeneous water column yet with noticeable differences between the 2 years (Figures 3 and 4). The temperature in the study area exhibited a range of 5.5°C at the seafloor to 7.1°C near the surface during CAGE 18-2. The average temperature during this cruise was 6.5 (standard deviation SD, 0.18) °C. In CAGE 22-3, the temperature ranged from 6.7°C near the seafloor to 8.0°C at the surface, with an average of 7.7 (SD, 0.07) °C. In CAGE 18-2, salinity levels varied between 34.28 and 35.05 psu, with an average of 34.52 (SD, 0.14) psu. During CAGE 22-3, salinity exhibited a slightly wider range of 34.12–35.10 psu, with an average of 34.96 (SD, 0.076) psu. The water column was mostly composed of NCW (low salinity) during CAGE 18-2 and of NAW during CAGE 22-3 (Figure 4) which is the most commonly found water mass in the area (Buhl-Mortensen et al., 2012). NCW flowed over NAW during CAGE 22-3 (Figure 3). The differences in water column characteristics between the two cruises, while occurring two to three weeks apart in 2018 and 2023, confirm the high oceanographic variability of the area.

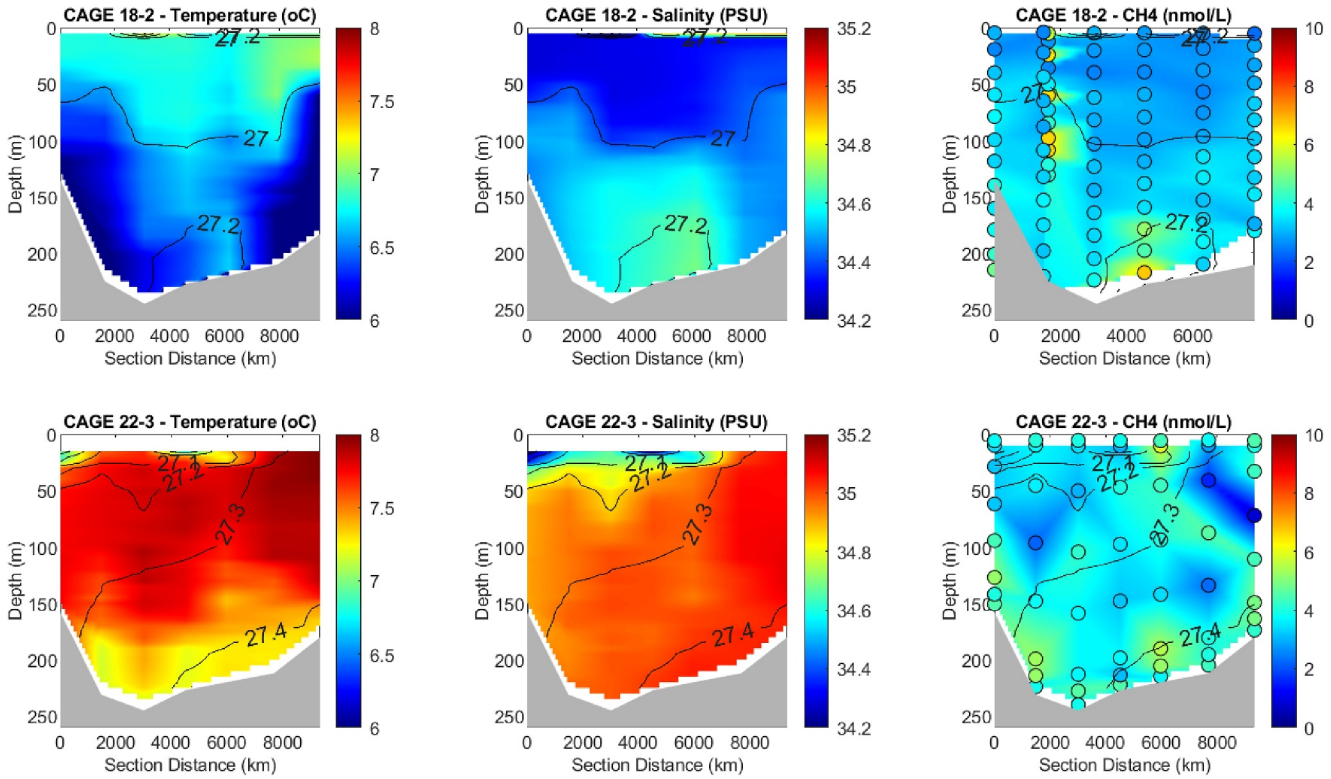


**Figure 3.** Temperature (left), salinity (center) and $CH_4$ concentration (right) along the transect of CTD 83 to 89 shown in Figure 1. The first line shows the measurements during CAGE 18-2 and the second line the measurements during CAGE 22-3. The color dots on the right figures are individual sample measurements at each depth, superimposed with the interpolated $CH_4$ concentrations.

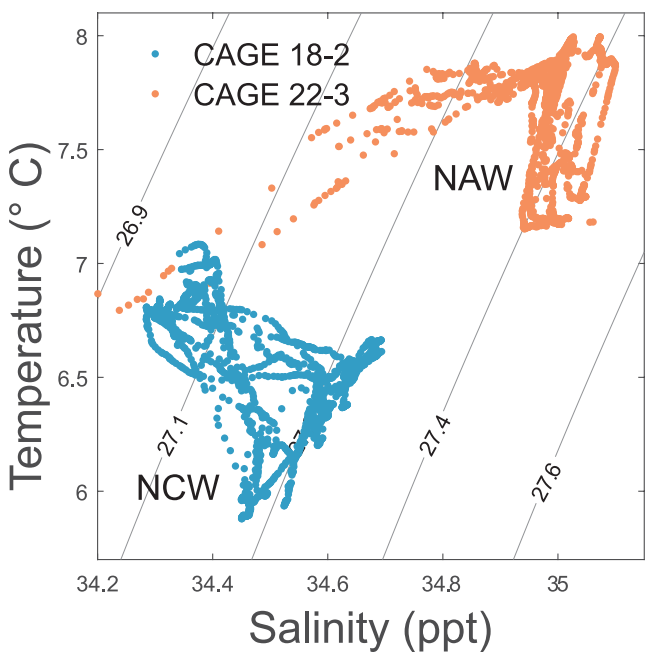


**Figure 4.** Temperature/Salinity (TS) diagram for both surveys (CAGE 18-2 in blue, CAGE 22-3 in orange). Isopycnic lines are indicated.

These oceanic conditions did not seem to affect the methane distribution in the water column, as both cruises exhibited low methane concentrations. However, methane concentrations were more localized and condensed during CAGE 18-2 than during CAGE 22-3 with a concentration range of 0.8–19 nM (average 3.5 (SD, 1.6) nM), whereas a more widespread distribution of methane was obtained during CAGE 22-3 varying from 0.8 to 7.5 nM (average 4.3 (SD, 1.4) nM) throughout the study area. Nevertheless, concentrations were low compared to other hydrocarbon seeps in the Arctic Ocean (e.g., offshore Svalbard) where it can reach up to a few thousand nM concentrations (Dølven et al., 2022).

### 4.3. Ocean Currents During CAGE 22-3

The ADCP data from the ship during CAGE 22-3 revealed a complex ocean circulation in the area, including eddies and tidal currents. The surface currents primarily flow in a northward direction with an average of 20.9 (SD, 16.3) cm $s^{-1}$, while the deeper currents exhibit more variability (Figure 5). The current average less than 5 m above the seafloor is 34.3 (SD, 72.6) cm $s^{-1}$ and can reach up to 1 m $s^{-1}$, which is a very strong current that could disturb the seafloor. These strong currents might therefore also explain the limited number of microbial mats and low water column concentrations despite the continuous seeping of $CH_4$ compared to other seepage areas (e.g., offshore Svalbard (Dessandier et al., 2019), Hikurangi Margin (Ruff et al., 2013), Hakon Mosby Mud Volcano in the Barents Sea (Niemann et al., 2006)).

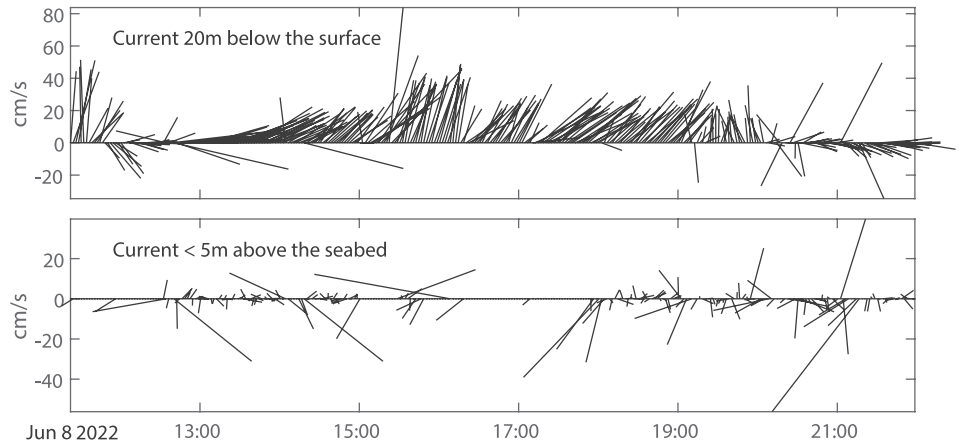


**Figure 5.** Current velocity near the surface (top) and less than five m above the seafloor (bottom).

### 4.4. Comparison of Flare Abundance, Locations and Properties

The complete overlap of MBES surveys, taking place at similar seasons of the year (end of May and beginning/mid-June), revealed a clear difference in activity, with CAGE 22-3 exhibiting 3.5 more flare observations compared to CAGE 18-2 (Figures 6 and 7, Table S2 in Supporting Information S1). We did not observe any flare reaching the sea surface, and the tallest flare observed reached 35 m below the sea surface. However, it is important to note that the acoustic signal could have been cut due to the opening angle of the MBES. Most of the flares were found at depths below 215 m depth. Specifically, the median depths for flares in CAGE 18-2 and CAGE 22-3 were approximately 219 and 215 m, respectively. The flare locations were primarily concentrated in three main areas, namely west of 14.263 E, east of 14.334 E, and an area in between as illustrated in Figure 1.

We also observed a large increase of seeps in water depths shallower than 150 m during CAGE 22-3 (Figures 6 and 7). The combined effect of a larger temperature increase at shallow depth (between 1.4 and 1.8°C increase near the seafloor at the northernmost and southernmost CTD stations vs. 0.8°C increase in the center of the Trough), and a decrease in hydrostatic pressure, will have a stronger effect on the sediment pore water at shallow sites (Römer et al., 2016).

Although the MBES were not calibrated and we can therefore not compare the signal amplitudes, this variable can inform on the amplitude distribution of the flares. Notably, it was predominantly within the range of −22 to −38 dB for both research cruises, mostly around 230 m depth (Figure 8, Table S2 in Supporting Information S1).

The different opening angles of the MBES during both cruises might influence the number of flares as a narrower opening angle during CAGE 22-3 implies a higher resolution. However, this resolution mainly concerns the outer beams and could only result in a better separation of potential overlap of flares, or a better detection of weaker flares. Here we combine flares that are less than 10 m away from each other, and Figure 8 clearly shows an increase of both strong and weak flares. Although a few weak flares might have been missed during CAGE 18-2, we can still consider our comparison of the two data sets robust despite the different settings.

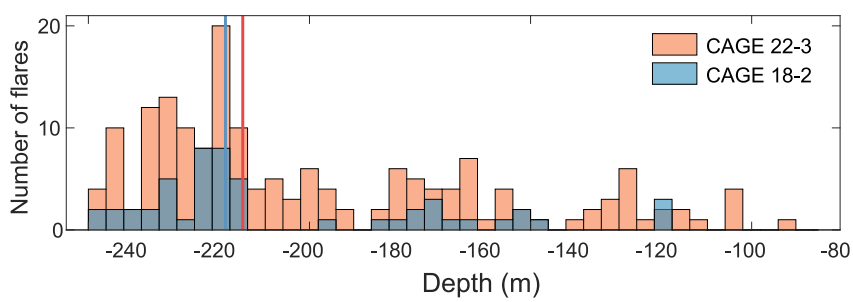


**Figure 6.** Flare density for both cruises with median depths of the flares.

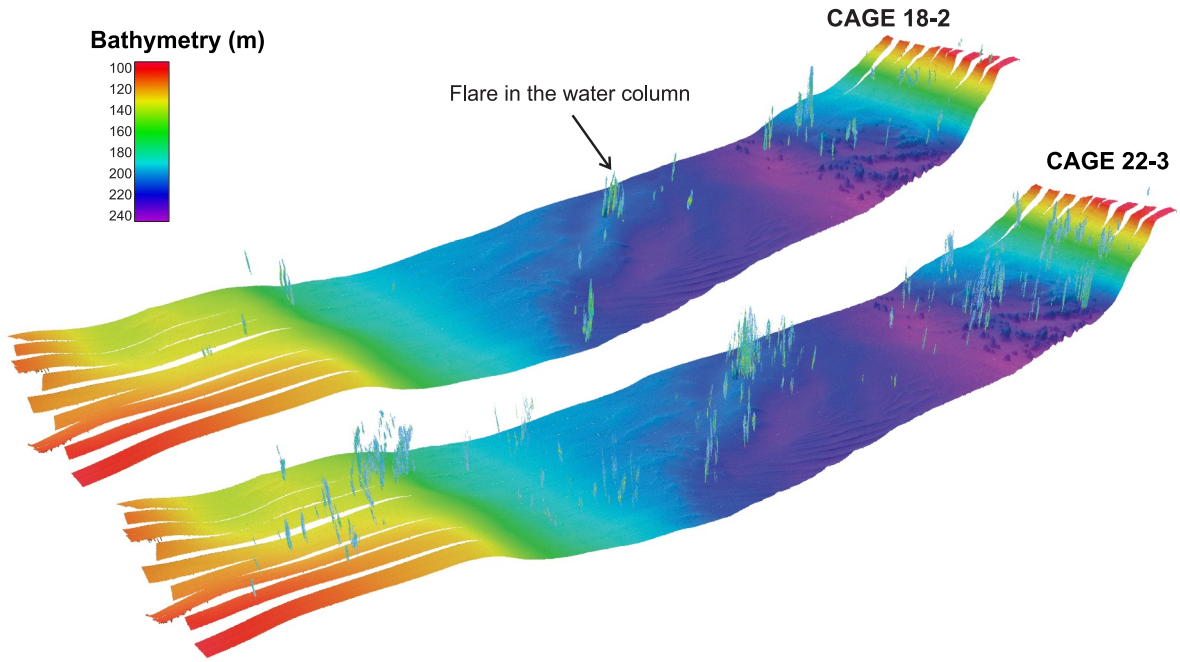


**Figure 7.** Flare representation in the water column from the MBES during CAGE 18-2 and CAGE 22-3 on top of the bathymetry. The flares are indicated.

The SBES survey performed during CAGE 18-2 revealed 43 clusters with flow rates ranging from 0.2 to 64 mL $min^{-1}$, an average of 14.4 (SD, 19.9) mL $min^{-1}$ and a median of 6.4 mL $min^{-1}$ (Figure 1). These values are smaller than other areas such as, for example, in the shallow Dutch Dogger Bank in the North Sea (from 0.43 to 2,148.5 mL $min^{-1}$, Römer et al., 2017 corrected after Veloso et al., 2019), near the gas hydrate stability limit offshore Svalbard (2.3–1,852 mL $min^{-1}$, Ferré et al., 2020), or in the South China Sea (94.8 mL $min^{-1}$ in average per flare, Zhang et al., 2023). Flares were emitted in the three main areas from an average depth of 206 m (median depth of 216 m ranging from 82 to 244 m), in agreement with the MBES data. The differences between the flares observed by the MBES and the SBES during CAGE 18-2 are explained by a larger observation angle from the MBES. Due to the narrow angle of the SBES (~7°), the distance between two adjacent line footprints ranged between approximately 60 m in the deepest areas (250 m depth) to around 20 m in the shallowest areas (80 m depth), whereas the MBES lines usually overlapped. In addition, the source of the flare is determined by the last coordinates the flare was observed, which can be different in both instruments.

The strong association between temperature fluctuations and seep activities at the gas hydrate stability zone (GHSZ) boundaries was previously shown (Ferré et al., 2020). Here, the increase in seep activity between CAGE

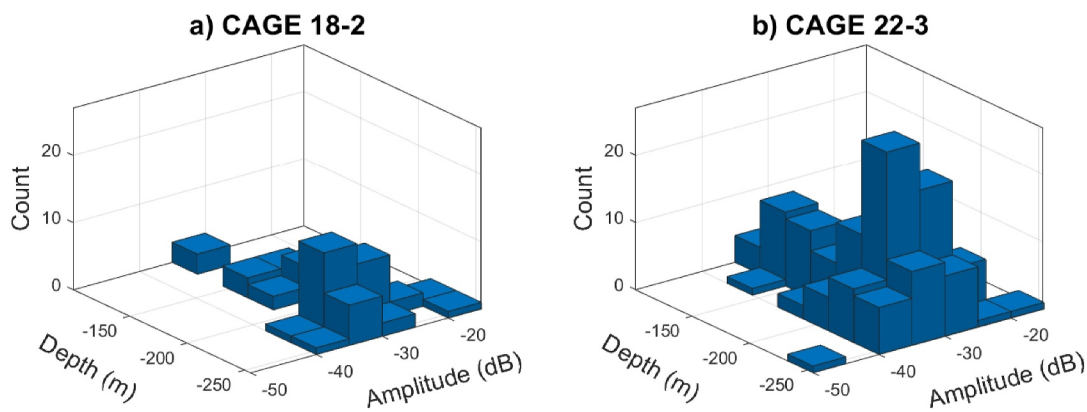


**Figure 8.** Histograms representing the flare numbers with regards to acoustic amplitude versus depth for both cruises.

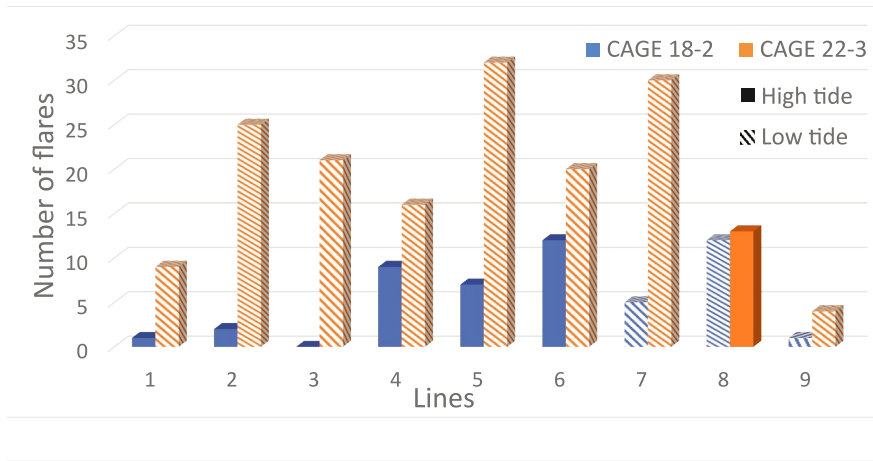


**Figure 9.** Histogram of the flare numbers at each line for each survey (blue for CAGE 18-2 and orange for CAGE 22-3), with the corresponding tide (full for high tide, striped for low tide). See Figure 1 for lines location.

18-2 and CAGE 22-3 could be linked to the temperature difference between these cruises, with bottom water temperature 1.2°C warmer during CAGE 22-3 compared to CAGE 18-2. However, based on the gas composition presented above and the water properties, our study area is always within the boundaries of the GHSZ. Indeed, we estimate the hydrate stability limit to fluctuate between ~312 m (at 5.5°C during CAGE 18-2) and 356 m (at 6.7°C during CAGE 22-3), both deeper than our study area (max ~250 m depth) (Figure S2 in Supporting Information S1). In addition, temperatures recorded at node 7 from September 2019 to June 2020 show a minimum of 6°C, indicating that the boundary of the GHSZ is most likely constantly below 312 m depth. Although we can conclude that the increased number of flares during CAGE 22-3 is not associated with a switch in GHSZ, the increase in bottom water temperature could lead to changes in gas solubility in sediment pore fluids which in turn could trigger methane release in the water column.

Pore pressure could also be indirectly affected by tidal changes, explaining different seep activities between the two cruises. Previous studies have shown that $CH_4$ release is influenced by tidal cycles due to the decreasing and increasing hydrostatic pressure (e.g., Boles et al., 2001; Römer et al., 2016; Sultan et al., 2020). We extracted the tide elevation during each MBES line from the TPXO tide model (Egbert & Erofeeva, 2002) at node 7, and compared it with the different flare locations during the two surveys. The tidal range during the study period was ~1 m. The tide was low during 3 out of 9 survey lines during CAGE 18-2 whereas it was low during 8 out of 9 lines during CAGE 22-3. Figure 9 provides insight into the number of flares observed on each line (cf. Figure 1 for line numbers) during both surveys, specifically during high and low tide. The data suggest a potential correlation between flare numbers and tidal conditions. Lines 1 to 6 show more flares during CAGE 22-3 which were performed at low tide, while line 8 exhibits a similar flare number during high tide in CAGE 22-3 and low tide in CAGE 18-2. Notably, line 7 stands out as an exception, with a much higher number of flares during CAGE 22-3 compared to CAGE 18-2 when the tide was low during both cruises. Line 9 presents a similar pattern at a lower extent. No clear pattern was observed when looking at increasing or decreasing tide.

Overall, these findings highlight the dynamic nature of $CH_4$ seepage in the study area, influenced by changing environmental conditions and seepage sources. It seems likely that the difference in seepage activity between the two cruises results in the combination of both temperature and tide, since they both influence the pore pressure and therefore the release of methane in the water column.

### 4.5. Surface and Sub-Seafloor Pore Pressure and Temperature

Data collected from the piezometer L01 short-term deployment are shown in Figure 10, that is, temperature (T) and pressure (P) at the surface sediment (index 1) and 3 m below the seafloor (index 2). In addition, we present the temperature and pressure extracted at node 7. Temperature variations are identical in all 3 temperature sensors (Figure 10b) and reflect changes in bottom water temperature. Note that T1 and T2 sensors record temperature at

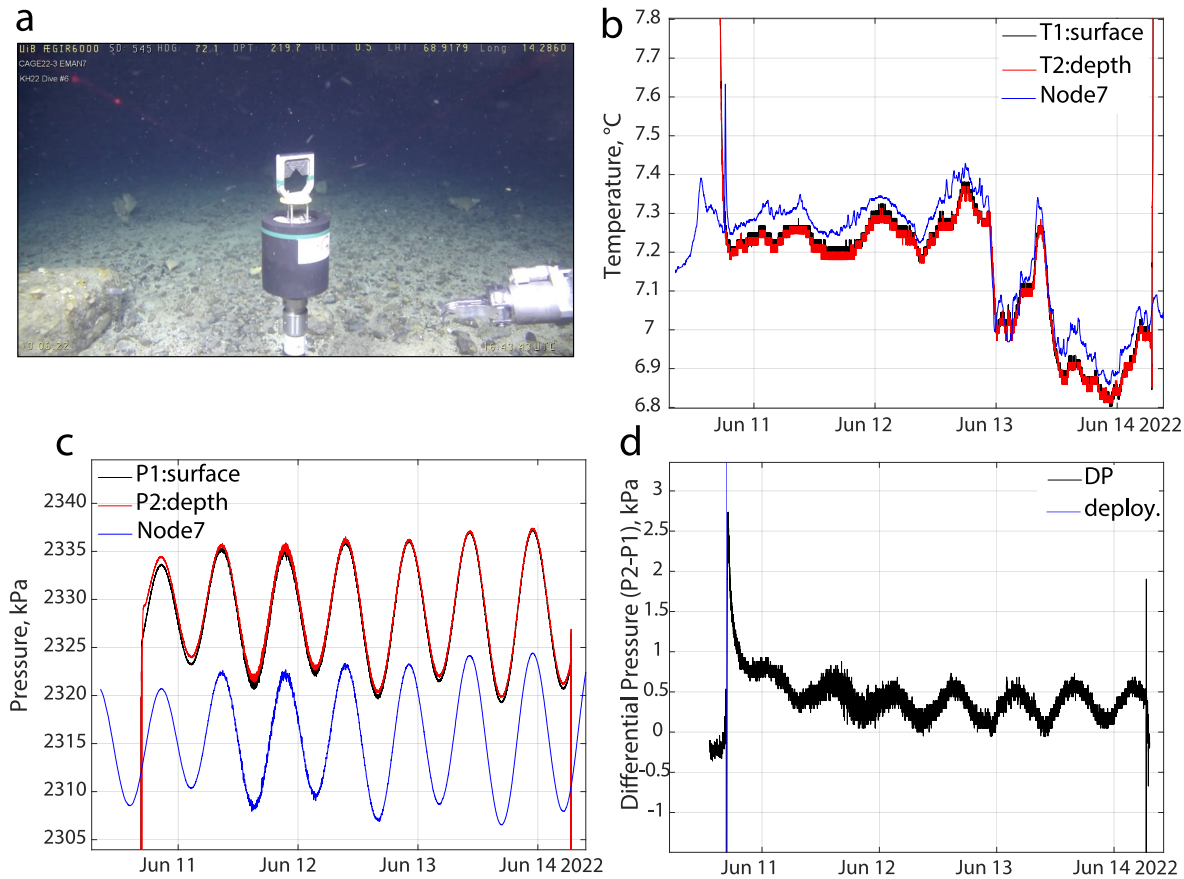


**Figure 10.** (a) Deployed piezometer—the logger head, hosting the sensors, with handle is plugged onto the standpipe. (b) Temperature for piezometer sensors T1 (black) and T2 (red), and for node 7 (blue). (c) Pressure for piezometer sensors P1 (black) and P2 (red), and at node 7 (blue). Note that P2 reflects pore pressure at depth (3 m). (d) Differential pressure (P2-P1). Deployment of the piezometer loggerhead is shown with the vertical blue line.

the pressure sensor ports that are both mounted on the instrument head, on top of the standpipe, hence the similarity. The 0.1°C offset with temperature data from node 7 likely reflects a sensor calibration issue.

The pressure variations differ by almost 15 kPa (Figure 10c) between the two data sets, that is, between the piezometer pressure P1 and P2 data and the node 7 pressure data. This is likely attributable to a sensor calibration issue as well for node 7 that needs further investigation. On the other hand, both piezometer P1 (seafloor bottom pressure) and P2 (compensated pressure in sediments, at 3 m) pressure recordings show similar variations (Figure 10c). The initial and final pressure fluctuations seen in P1 (black) and P2 (red) (Figure 10c) are the ROV handling of the sensor head before mating with the standpipe. It stops immediately for the surface sensor P1 once the mating is complete; the response of the down port (P2) is slower due to the long standpipe but gradually building up to slightly higher (compensated) pressure than measured at the surface, that is, slightly excess (positive) pore. This is also reflected when calculating the in situ pore pressure, that is, the differential pressure between P1 and P2.

The in situ pore pressure record comprises three distinct components (Figure 10d). The early part of the recording is dominated by the decay of the pressure pulse associated with the standpipe penetration. The rate of decay of this pulse can be used to estimate in situ permeability (e.g., Fang et al., 1993; and references therein). The record also exhibits periodic oscillation that is associated with tidal pressure variation on the seafloor. The amplitude and phase of these oscillations, when compared to the tidal forcing function, can be used to derive in situ permeability (e.g., Van Der Kamp & Gale, 1983; Wang & Davis, 1996). The last component is the ambient equilibrium (baseline) pore pressure, which for the L01 record is positive with respect to hydrostatic reflecting an over pore pressure (in excess) in the sediment.

Overall, these preliminary results from the short-term deployment confirm, as hypothesized, both the over-pressurized (excess pore pressure) sediments, likely due to the presence of gas, and the time-dependent pore pressure perturbation resulting from the tidal forcing. We aim at using the latter in combination with the long-term deployment data to constrain phase lag between pore pressure and the tidal loading signal, the present study is outside of this scope. Long-term deployment data will be favored for this analysis as more data (i.e., more tidal cycles) will strengthen the phase estimate stability. Ultimately, because the magnitude of these phase lags depends upon the system's poroelastic parameters, we will constrain the associated effective permeability of the system.

### 4.6. Gas Accumulation and Migration From Sub-Bottom Profiler

The bathymetry and SBP data show that node seven is located on the eastern slope of a subtle ridge structure that is extending in N-S direction deepening toward the North (Figures 1 and 11). Two large CWC mounds are located at the top of the ridge and hydroacoustic data show high intensity of gas seepage between CWC mounds and node 7. The SBP data shows several high-amplitude anomalies in the subsurface varying from 1 to 15 m below the seafloor (Figure 11). They form an irregular patchy pattern along almost the whole of both lines (cf. location in Figure 1). Sedimentary reflections are visible toward the eastern part of the lines in what appears to be a small basin structure. Any coherent energy is absent beneath the high-amplitude reflections. The acoustic character and distribution of high-amplitude anomalies suggest that they are a consequence of the presence of gas in the shallow subsurface. The observation of gas accumulations at a few meters below the seafloor corroborates the existence of overpressure from pore-pressure measurements. The patchy occurrence and depth distribution of gas accumulations also appear consistent with varying depths of the sulfate–$CH_4$-transition zone (SMTZ) between 80 cm and >250 cm indicating spatially heterogeneous $CH_4$ ascent (Sauer et al., 2015). The presence of gas causes all acoustic energy to attenuate, creating a blanked, transparent zone underneath, where no subsurface structure is visible.

Gas accumulations are arranged in a way that indicates gas migration (light blue arrows) from depth updip and laterally toward the shallowest point of the seafloor (Figure 11). The seafloor reflection of the SBP data is broken up or reduced in areas where gas seepage has been detected. Here, the gas column reaches all the way to the seabed and gas seeps into the water column diminishing acoustic impedance contrasts at the seafloor. Gas migration shows a topographical control focusing toward small local highs in the seafloor morphology. Also, gas seeps identified outside of SBP coverage show a correlation with small positive structures in the seafloor morphology indicating that topography is a dominant mechanism for gas migration in the shallow subsurface (Figure 1b).

## 5. Conclusions

We presented some findings from the EMAN7 project, comparing data obtained during two research cruises (CAGE 18-2 in May 2018 and CAGE 22-3 in June 2022). Our findings highlighted.

1. a substantial variability in $CH_4$ activity between the two cruises (3.5 times more during CAGE 22-3) that occurred at a similar period of the year (May/June). A combination of temperature and tide conditions seems to be linked to our observations, since the bottom temperature was 1.2°C higher and the tide mostly low during CAGE 22-3 where we observed the highest activity. In addition, tide in the area is felt up to 3 m below the sediment, which corroborates with a strong effect on the short-term variability of $CH_4$ release.
2. the presence of microbial mats on the seafloor, although these were not as extensive as in other study areas (e.g., Dessandier et al., 2019). This could be explained by intermittent seep activity which prevents the formation of microbial mats, or potentially by a strong local current that disturbs the seafloor. This strong current also explains the low methane concentration in the water column during both research cruises.
3. the presence of gas and gas migration pathways toward the surface sediment at locations where $CH_4$ seeps were found, as revealed from sub-seafloor observations. This gas migration is steered by topography in the area.

The large difference in $CH_4$ activity, exceeding 110% between two research cruises conducted during the same season but four years apart, precludes us from proposing annual flow rates for the area. Long oceanographic and geochemistry time series obtained at node 7 should help elucidate this.

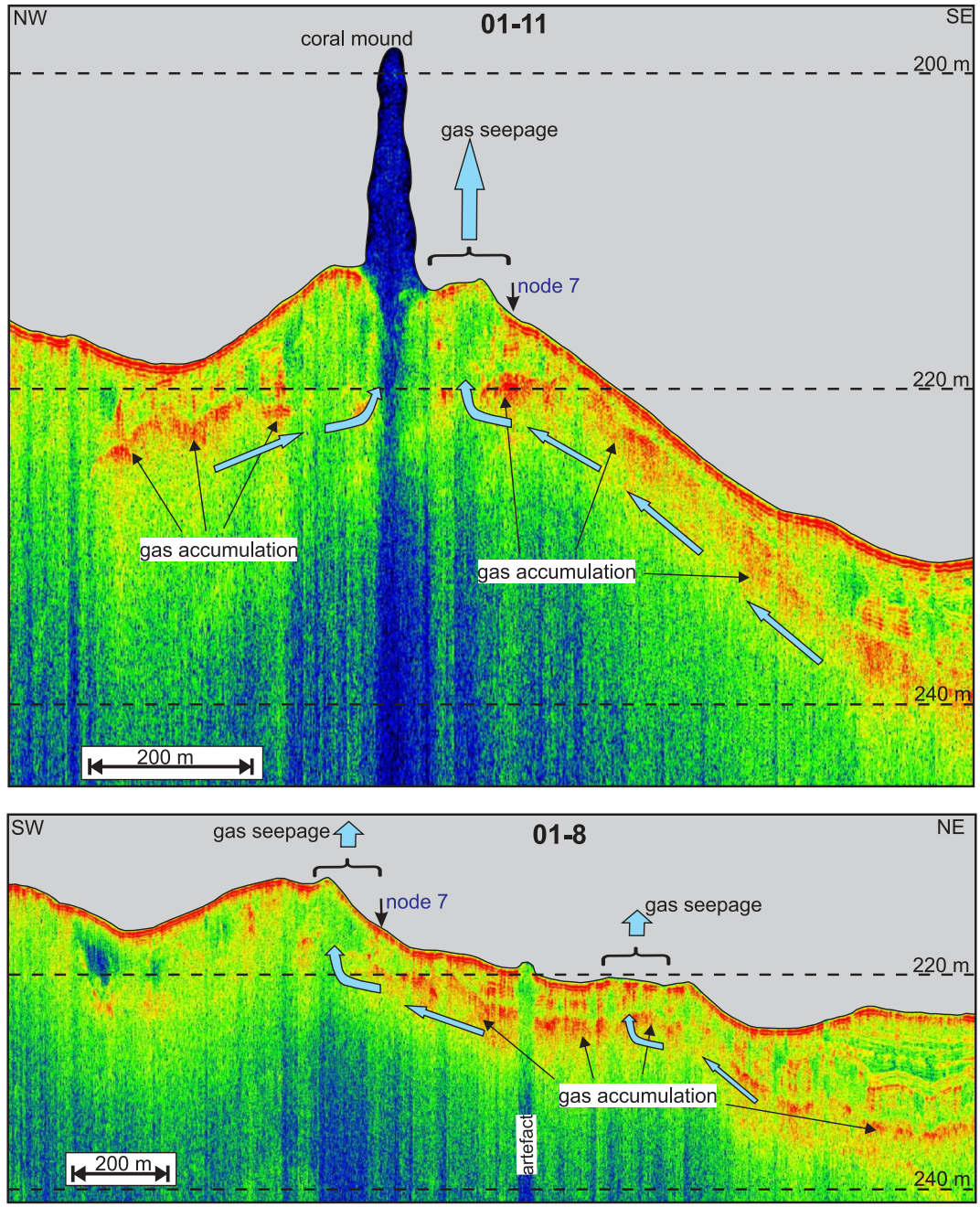


**Figure 11.** Sub-sediment profiles obtained from the SBP along the lines 01–8 and 01–11 during CAGE 22-3 as indicated in Figure 1. Line 01–11 crosses the northern coral mound as well as CH4 seeps.

## Data Availability Statement

All data used in this manuscript is available on the platform Open Research Data at the University of Tromsø—The Arctic University of Norway (https://doi.org/10.18710/FCINC0) (Ferré et al., 2024). The clustering code can be found here: https://zenodo.org/records/11214460 (Dølven, 2024). The tides were extracted via request on the website https://tpxows.azurewebsites.net/ (Egbert & Erofeeva, 2002).

**Acknowledgments**
This study is funded by the Research Council of Norway through CAGE (Centre for Arctic Gas Hydrate, Environment and Climate) project number 223259 and EMAN7 (Environmental impact of Methane seepage and sub-seabed characterization at LoVe-Node 7) project number 320100. We thank the crew of R/Vs *Helmer Hanssen* during CAGE 18-2 and *Kronprins Haakon* during CAGE 22-3, as well as the crew of the ROV *Ægir6000*.

## References

Archer, D., Buffett, B., & Brovkin, V. (2009). Ocean methane hydrates as a slow tipping point in the global carbon cycle. *Proceedings of the National Academy of Sciences of the U S A*, *106*(49), 20596–20601. https://doi.org/10.1073/pnas.0800885105

Argentino, C., Savini, A., & Panieri, G. (2022). Integrating fine-scale habitat mapping and pore water analysis in cold seep research: A case study from the SW Barents Sea. In J. Mienert, C. Berndt, A. M. Tréhu, A. Camerlenghi, & C.-S. Liu (Eds.), *World atlas of submarine gas hydrates in continental margins* (pp. 505–514). Springer International Publishing.

Barreyre, T., Escartín, J., Garcia, R., Cannat, M., Mittelstaedt, E., & Prados, R. (2012). Structure, temporal evolution, and heat flux estimates from the Lucky Strike deep-sea hydrothermal field derived from seafloor image mosaics. *Geochemistry, Geophysics, Geosystems*, *13*(4), Q04007. https://doi.org/10.1029/2011GC003990

Barreyre, T., Olive, J. A., Crone, T. J., & Sohn, R. A. (2018). Depth-dependent permeability and heat output at Basalt-hosted hydrothermal systems across mid-ocean ridge spreading rates. *Geochemistry, Geophysics, Geosystems*, *19*(4), 1259–1281. https://doi.org/10.1002/2017gc007152

Becker, E. L., Cordes, E. E., Macko, S. A., & Fisher, C. R. (2009). Importance of seep primary production to Lophelia pertusa and associated fauna in the Gulf of Mexico. *Deep Sea Research Part I: Oceanographic Research Papers*, *56*(5), 786–800. https://doi.org/10.1016/j.dsr.2008.12.006

Berndt, C., Feseker, T., Treude, T., Krastel, S., Liebetrau, V., Niemann, H., et al. (2014). Temporal constraints on hydrate-controlled methane seepage off Svalbard. *Science*, *343*(6168), 284–287. https://doi.org/10.1126/science.1246298

Biastoch, A., Treude, T., Rüpke, L. H., Riebesell, U., Roth, C., Burwicz, E. B., et al. (2011). Rising Arctic Ocean temperatures cause gas hydrate destabilization and ocean acidification. *Geophysical Research Letters*, *38*(8), L08602. https://doi.org/10.1029/2011gl047222

Bindoff, N. L., Cheung, W. W. L., Kairo, J. G., Arístegui, J., Guinder, V. A., Hallberg, R., et al. (2019). Changing Ocean, marine ecosystems, and dependent communities. In D. C. R. H.-O. Pörtner, V. Masson-Delmotte, P. Zhai, M. Tignor, E. Poloczanska, K. Mintenbeck, et al. (Eds.), *IPCC special report on the ocean and cryosphere in a changing climate* (pp. 447–587). Cambridge University Press.

Blindheim, J. (1990). Arctic intermediate water in the Norwegian Sea. *Deep-Sea Research, Part A: Oceanographic Research Papers*, *37*(9), 1475–1489. https://doi.org/10.1016/0198-0149(90)90138-I

Bøe, R., Bellec, V., Dolan, M., Buhl-Mortensen, P., Buhl-Mortensen, L., Slagstad, D., & Rise, L. (2009). Giant sandwaves in the Hola glacial trough off Vesterålen, North Norway. *Marine Geology*, *267*(1–2), 36–54. https://doi.org/10.1016/j.margeo.2009.09.008

Boetius, A., & Wenzhöfer, F. (2013). Seafloor oxygen consumption fuelled by methane from cold seeps. *Nature Geoscience*, *6*(9), 725–734. https://doi.org/10.1038/ngeo1926

Boles, J. R., Clark, J. F., Leifer, I., & Washburn, L. (2001). Temporal variation in natural methane seep rate due to tides, Coal Oil Point area, California. *Journal of Geophysical Research*, *106*(C11), 27077–27086. https://doi.org/10.1029/2000jc000774

Børve, E., Isachsen, P. E., & Nøst, O. A. (2021). Rectified tidal transport in Lofoten–Vesterålen, northern Norway. *Ocean Science*, *17*(6), 1753–1773. https://doi.org/10.5194/os-17-1753-2021

Buhl-Mortensen, L., Bøe, R., Dolan, M. F. J., Buhl-Mortensen, P., Thorsnes, T., Elvenes, S., & Hodnesdal, H. (2012). Banks, troughs, and canyons on the continental margin off Lofoten, Vesterålen, and Troms, Norway. In *Seafloor Geomorphology as benthic habitat* (pp. 703–715).

Chand, S., Mienert, J., Andreassen, K., Knies, J., Plassen, L., & Fotland, B. (2008). Gas hydrate stability zone modelling in areas of salt tectonics and pockmarks of the Barents Sea suggests an active hydrocarbon venting system. *Marine and Petroleum Geology*, *25*(7), 625–636. https://doi.org/10.1016/j.marpetgeo.2007.10.006

Cremiere, A., Lepland, A., Chand, S., Sahy, D., Condon, D. J., Noble, S. R., et al. (2016). Timescales of methane seepage on the Norwegian margin following collapse of the Scandinavian Ice Sheet. *Nature Communications*, *7*(1), 11509. https://doi.org/10.1038/ncomms11509

Damm, E., Mackensen, A., Budéus, G., Faber, E., & Hanfland, C. (2005). Pathways of methane in seawater: Plume spreading in an Arctic shelf environment (SW-Spitsbergen). *Continental Shelf Research*, *25*(12), 1453–1472. https://doi.org/10.1016/j.csr.2005.03.003

Dessandier, P.-A., Borrelli, C., Kalenitchenko, D., & Panieri, G. (2019). Benthic foraminifera in Arctic methane hydrate bearing sediments. *Frontiers in Marine Science*, *6*, 765. https://doi.org/10.3389/fmars.2019.00765

Dølven, K. O. (2024). Flare clustering [Software]. *Zenodo*. https://doi.org/10.5281/zenodo.11214460

Dølven, K. O., Ferré, B., Silyakova, A., Jansson, P., Linke, P., & Moser, M. (2022). Autonomous methane seep site monitoring offshore western Svalbard: Hourly to seasonal variability and associated oceanographic parameters. *Ocean Science*, *18*(1), 233–254. https://doi.org/10.5194/os-18-233-2022

Egbert, G. D., & Erofeeva, S. Y. (2002). Efficient inverse modeling of barotropic ocean tides. *Journal of Atmospheric and Oceanic Technology*, *19*(2), 183–204. https://doi.org/10.1175/1520-0426(2002)019<0183:EIMOBO>2.0.CO;2

Fallati, L., Panieri, G., Argentino, C., Varzi, A. G., Bünz, S., & Savini, A. (2023). Characterizing Håkon Mosby Mud Volcano (Barents Sea) cold seep systems by combining ROV-based acoustic data and underwater photogrammetry. *Frontiers in Marine Science*, *10*, 1269197. https://doi.org/10.3389/fmars.2023.1269197

Fallati, L., Saponari, L., Savini, A., Marchese, F., Corselli, C., & Galli, P. (2020). Multi-temporal UAV data and object-based image analysis (OBIA) for estimation of substrate changes in a post-bleaching scenario on a Maldivian reef. *Remote Sensing*, *12*(13), 2093. https://doi.org/10.3390/rs12132093

Fang, W. W., Langseth, M. G., & Schultheiss, P. J. (1993). Analysis and application of in situ pore pressure measurements in marine sediments. *Journal of Geophysical Research*, *98*(B5), 7921–7938. https://doi.org/10.1029/93JB00153

Ferré, B., Barreyre, T., Bünz, S., Argentino, C., Corrales-Guerrero, J., Dølven, K. O., et al. (2024). Replication Data for: Contrasting methane seepage dynamics in Hola trough offshore Norway: Insights from two different summers [Dataset]. https://doi.org/10.18710/FCINC0

Ferré, B., Jansson, P. G., Moser, M., Serov, P., Portnov, A., Graves, C. A., et al. (2020). Reduced methane seepage from Arctic sediments during cold bottom-water conditions. *Nature Geoscience*, *13*(2), 144–148. https://doi.org/10.1038/s41561-019-0515-3

Ferré, B., Mienert, J., & Feseker, T. (2012). Ocean temperature variability for the past 60 years on the Norwegian-Svalbard margin influences gas hydrate stability on human time scales. *Journal of Geophysical Research*, *117*(C10), C10017. https://doi.org/10.1029/2012JC008300

Franek, P., Plaza-Faverola, A., Mienert, J., Buenz, S., Ferré, B., & Hubbard, A. (2017). Microseismicity linked to gas migration and leakage on the western Svalbard shelf. *Geochemistry, Geophysics, Geosystems*, *18*(12), 4623–4645. https://doi.org/10.1002/2017gc007107

Hovland, M., Mortensen, P. B., Brattegard, T., Strass, P., & Rokengen, K. (1998). Ahermatypic coral banks off mid-Norway; evidence for a link with seepage of light hydrocarbons. *PALAIOS*, *13*(2), 189–200. https://doi.org/10.2307/3515489

Jensen, S., Bourne, D. G., Hovland, M., & Colin Murrell, J. (2012). High diversity of microplankton surrounds deep-water coral reef in the Norwegian Sea. *FEMS Microbiology Ecology*, *82*(1), 75–89. https://doi.org/10.1111/j.1574-6941.2012.01408.x

Judd, A., & Hovland, M. (2007). *Seabed fluid flow: The impact on geology, biology and the marine environment*. Cambridge University Press.

Ladroit, Y., Escobar-Flores, P. C., Schimel, A. C. G., & O'Driscoll, R. L. (2020). ESP3: An open-source software for the quantitative processing of hydro-acoustic data. *SoftwareX*, *12*, 100581. https://doi.org/10.1016/j.softx.2020.100581

Leifer, I., & Patro, R. K. (2002). The bubble mechanism for methane transport from the shallow sea bed to the surface: A review and sensitivity study. *Continental Shelf Research*, *22*(16), 2409–2428. https://doi.org/10.1016/S0278-4343(02)00065-1

Lim, A., Wheeler, A. J., Price, D. M., O'Reilly, L., Harris, K., & Conti, L. (2020). Influence of benthic currents on cold-water coral habitats: A combined benthic monitoring and 3D photogrammetric investigation. *Scientific Reports*, *10*(1), 19433. https://doi.org/10.1038/s41598-020-76446-y

Loeng, H. (1991). Features of the physical oceanographic conditions of the Barents Sea. *Polar Research*, *10*(1), 5–18. https://doi.org/10.1111/j.1751-8369.1991.tb00630.x

McGinnis, D. F., Greinert, J., Artemov, Y., Beaubien, S. E., & Wüest, A. (2006). Fate of rising methane bubbles in stratified waters: How much methane reaches the atmosphere? *Journal of Geophysical Research*, *111*(C9), C09007. https://doi.org/10.1029/2005JC003183

Misund, O. A., & Olsen, E. (2013). LofotenVesterlen: For cod and cod fisheries, but not for oil? *ICES Journal of Marine Science*, *70*(4), 722–725. https://doi.org/10.1093/icesjms/fst086

Myhre, C. L., Ferré, B., Platt, S. M., Silyakova, A., Hermansen, O., Allen, G., et al. (2016). Extensive release of methane from Arctic seabed west of Svalbard during summer 2014 does not influence the atmosphere. *Geophysical Research Letters*, *43*(9), 4624–4631. https://doi.org/10.1002/2016GL068999

Myhre, G., Shindell, D., Breon, F. M., Collins, W., Fuglestvedt, J., Huang, J. P., et al. (2013). Anthropogenic and natural radiative forcing. *Climate Change 2013: The Physical Science Basis*, 659–740.

Niemann, H., Losekann, T., de Beer, D., Elvert, M., Nadalig, T., Knittel, K., et al. (2006). Novel microbial communities of the Haakon Mosby mud volcano and their role as a methane sink. *Nature*, *443*(7113), 854–858. https://doi.org/10.1038/nature05227

Orr, J. C., Fabry, V. J., Aumont, O., Bopp, L., Doney, S. C., Feely, R. A., et al. (2005). Anthropogenic ocean acidification over the twenty-first century and its impact on calcifying organisms. *Nature*, *437*(7059), 681–686. https://doi.org/10.1038/nature04095

Panieri, G., Argentino, C., Ramalho, S. P., Vulcano, F., Savini, A., Fallati, L., et al. (2024). An Arctic natural oil seep investigated from space to the seafloor. *Science of the Total Environment*, *907*, 167788. https://doi.org/10.1016/j.scitotenv.2023.167788

Price, D. M., Robert, K., Callaway, A., Lo Iacono, C., Hall, R. A., & Huvenne, V. A. I. (2019). Using 3D photogrammetry from ROV video to quantify cold-water coral reef structural complexity and investigate its influence on biodiversity and community assemblage. *Coral Reefs*, *38*(5), 1007–1021. https://doi.org/10.1007/s00338-019-01827-3

Römer, M., Riedel, M., Scherwath, M., Heesemann, M., & Spence, G. D. (2016). Tidally controlled gas bubble emissions: A comprehensive study using long-term monitoring data from the NEPTUNE cabled observatory offshore Vancouver island. *Geochemistry, Geophysics, Geosystems*, *17*(9), 3797–3814. https://doi.org/10.1002/2016gc006528

Römer, M., Wenau, S., Mau, S., Veloso-Alarcon, M., Greinert, J., Schlüter, M., & Bohrmann, G. (2017). Assessing marine gas emission activity and contribution to the atmospheric methane inventory: A multidisciplinary approach from the Dutch Dogger Bank seep area (North Sea). *Geochemistry, Geophysics, Geosystems*, *18*(7), 2617–2633. https://doi.org/10.1002/2017GC006995

Ruff, S. E., Arnds, J., Knittel, K., Amann, R., Wegener, G., Ramette, A., & Boetius, A. (2013). Microbial communities of deep-sea methane seeps at Hikurangi continental margin (New Zealand). *PLoS One*, *8*(9), e72627. https://doi.org/10.1371/journal.pone.0072627

Sauer, S., Crémière, A., Knies, J., Lepland, A., Sahy, D., Martma, T., et al. (2017). U-Th chronology and formation controls of methane-derived authigenic carbonates from the Hola trough seep area, northern Norway. *Chemical Geology*, *470*, 164–179. https://doi.org/10.1016/j.chemgeo.2017.09.004

Sauer, S., Knies, J., Lepland, A., Chand, S., Eichinger, F., & Schubert, C. J. (2015). Hydrocarbon sources of cold seeps off the Vesterålen coast, northern Norway. *Chemical Geology*, *417*, 371–382. https://doi.org/10.1016/j.chemgeo.2015.10.025

Saunois, M., Stavert, A. R., Poulter, B., Bousquet, P., Canadell, J. G., Jackson, R. B., et al. (2020). The global methane budget 2000–2017. *Earth System Science Data*, *12*(3), 1561–1623. https://doi.org/10.5194/essd-12-1561-2020

Sen, A., Himmler, T., Hong, W. L., Chitkara, C., Lee, R. W., Ferre, B., et al. (2019). Atypical biological features of a new cold seep site on the Lofoten-Vesteralen continental margin (northern Norway). *Scientific Reports*, *9*(1), 1762. https://doi.org/10.1038/s41598-018-38070-9

Shakhova, N., Semiletov, I., Salyuk, A., Yusupov, V., Kosmach, D., & Gustafsson, Ö. (2010). Extensive methane venting to the atmosphere from sediments of the East Siberian Arctic Shelf. *Science*, *327*(5970), 1246–1250. https://doi.org/10.1126/science.1182221

Sibuet, M., & Roy, K. O. L. (2002). Cold seep communities on continental margins: Structure and Quantitative distribution relative to geological and fluid venting patterns. In *Ocean margin systems* (pp. 235–251). Springer Berlin Heidelberg.

Silyakova, A., Jansson, P., Serov, P., Ferré, B., Pavlov, A. K., Hattermann, T., et al. (2020). Physical controls of dynamics of methane venting from a shallow seep area west of Svalbard. *Continental Shelf Research*, *194*, 104030. https://doi.org/10.1016/j.csr.2019.104030

Sultan, N., Plaza-Faverola, A., Vadakkepuliyambatta, S., Buenz, S., & Knies, J. (2020). Impact of tides and sea-level on deep-sea Arctic methane emissions. *Nature Communications*, *11*(1), 5087. https://doi.org/10.1038/s41467-020-18899-3

Van Der Kamp, G., & Gale, J. E. (1983). Theory of earth tide and barometric effects in porous formations with compressible grains. *Water Resources Research*, *19*(2), 538–544. https://doi.org/10.1029/WR019i002p00538

Veloso, M., Greinert, J., Mienert, J., & De Batist, M. (2015). A new methodology for quantifying bubble flow rates in deep water using splitbeam echosounders: Examples from the Arctic offshore NW-Svalbard. *Limnology and Oceanography: Methods*, *13*(6), 267–287. https://doi.org/10.1002/lom3.10024

Veloso, M., Greinert, J., Mienert, J., & De Batist, M. (2019). Corrigendum: A new methodology for quantifying bubble flow rates in deep water using splitbeam echosounders: Examples from the Arctic offshore NW-Svalbard. *Limnology and Oceanography: Methods*, *17*(2), 177–178. https://doi.org/10.1002/lom3.10313

Wang, K., & Davis, E. E. (1996). Theory for the propagation of tidally induced pore pressure variations in layered subseafloor formations. *Journal of Geophysical Research*, *101*(B5), 11483–11495. https://doi.org/10.1029/96JB00641

Whiticar, M. J. (1999). Carbon and hydrogen isotope systematics of bacterial formation and oxidation of methane. *Chemical Geology*, *161*(1), 291–314. https://doi.org/10.1016/S0009-2541(99)00092-3

Wiesenberg, D. A., & Guinasso, N. L. (1979). Equilibrium solubilities of methane, carbon monoxide, and hydrogen in water and sea water. *Journal of Chemical & Engineering Data*, *24*(4), 356–360. https://doi.org/10.1021/je60083a006

Zhang, K., Song, H., Chen, J., Geng, M., & Liu, B. (2023). Gas seepage detection and gas migration mechanisms. In D. Chen & D. Feng (Eds.), *South China sea seeps* (pp. 35–53). Springer Nature Singapore.